ELSEVIER

Near-Earth Asteroid 2005 CR37: Radar images and photometry of a candidate contact binary

Lance A.M. Benner [a,*], Michael C. Nolan [b], Steven J. Ostro [a], Jon D. Giorgini [a], Donald P. Pray [c], Alan W. Harris [d], Christopher Magri [e], Jean-Luc Margot [f]

[a] *Jet Propulsion Laboratory, California Institute of Technology, 4800 Oak Grove Drive, Pasadena, CA 91109, USA*
[b] *National Astronomy and Ionosphere Center, Arecibo Observatory, HC3 Box 53995, Arecibo, PR 00612, USA*
[c] *Carbuncle Hill Observatory, P.O. Box 946, Coventry, RI 02816, USA*
[d] *Space Science Institute, 4603 Orange Knoll Avenue, La Canada, CA 91011, USA*
[e] *University of Maine at Farmington, 39 High Street, Preble Hall, Farmington, ME 04938, USA*
[f] *Department of Astronomy, Cornell University, Ithaca, NY 15853, USA*

Abstract

Arecibo (2380 MHz, 13 cm) radar observations of 2005 CR37 provide detailed images of a candidate contact binary: a 1.8-km-long, extremely bifurcated object. Although the asteroid's two lobes are round, there are regions of modest topographic relief, such as an elevated, 200-m-wide facet, that suggest that the lobes are geologically more complex than either coherent fragments or homogeneous rubble piles. Since January 1999, about 9% of NEAs larger than ∼200 m imaged by radar can be described as candidate contact binaries.
© 2006 Elsevier Inc. All rights reserved.

Keywords: Asteroids; Radar; Surfaces, asteroids; Asteroids, composition

1. Observations and orbit refinement

2005 CR37 was discovered by H. Mikuz at Crni Vrh Observatory (Slovenia) on February 8, 2005 (M.P.E.C. 2005-C32, http://cfa-www.harvard.edu/iau/mpec/K05/K05C32.html). It immediately became clear that the object would make a close approach to Earth and, given its estimated absolute magnitude, $H = 18.9$, would be a very strong radar target.

We observed it at Arecibo during a 2.3-h interval on February 23; see Benner et al. (1999a, 1999b, 2002a) and Ostro et al. (1983, 1996) for discussion of radar techniques. The radar's nominal parameters were: transmit frequency = 2380 MHz, transmitter power = 700 kW, OC system temperature = 24 K. We started with five "Doppler-only," continuous wave (CW) transmit-receive cycles (runs), measured a correction to the ephemeris, updated it, and did another CW run with the new

Table 1
Radar observations

Setup	Code	OSOD	Runs	Start	Stop
CW		14	5	04:03:41	04:14:25
CW		16	1	04:18:00	04:19:04
4.0 µs	8191	16	2	04:27:42	04:31:10
4.0 µs	1023	16	1	04:34:11	04:35:15
0.1 µs	65535	16	38	04:43:01	06:18:47

Columns give the radar setup, the code length for the repetitive binary-phase-coded transmission in imaging setups, the orbit solution computed using the JPL On-Site Orbit Determination (OSOD) software, the number of transmit-receive cycles (runs), and the start and stop UTC epochs of echo reception.

ephemeris to verify the accuracy of its Doppler prediction. We then used setups with a time-delay resolution of 4 µs (600 m) to measure the asteroid's range and concluded with 38 0.1-µs (15-m) imaging runs (Table 1).

Prior to radar detection, the 3σ uncertainties on 2005 February 26.0 were 180 Hz and 0.33 s (49,000 km). We used the coarse-resolution 4-µs ranging and high-resolution 0.1-µs imaging data to estimate two range corrections to the ephemeris. The

Table 2
Close approaches

Date			Body	Close approach distance			V_{rel} (km s^{-1})	TCA3Sg (min)
				Nominal (AU)	Minimum (AU)	Maximum (AU)		
1784	Feb	24.49926	Earth	0.0741	0.0689	0.1212	16.487	5332.5
1834	Feb	26.04014	Earth	0.0687	0.0685	0.0709	16.255	1036.5
1884	Feb	26.28389	Earth	0.0675	0.0672	0.0680	16.299	221.62
1934	Feb	24.45044	Earth	0.0851	0.0836	0.0867	16.836	168.11
2005	Feb	26.78912	Earth	0.0628	0.0628	0.0628	16.246	0.03
2076	Feb	25.30258	Earth	0.0742	0.0728	0.0756	16.748	175.28
2168	Feb	26.56139	Earth	0.0692	0.0681	0.0703	16.649	158.85
2260	Feb	28.77030	Earth	0.0586	0.0586	0.0586	16.330	0.83
2276	Aug	26.01656	Vesta	0.0677	0.0672	0.0682	11.806	7.32
2352	Mar	05.62895	Earth	0.0994	0.0980	0.1008	15.346	145.31
2352	Nov	14.27555	Vesta	0.0362	0.0354	0.0369	12.299	39.74
2423	Mar	04.81276	Earth	0.0786	0.0774	0.0799	15.560	148.95
2494	Mar	05.81731	Earth	0.0955	0.0932	0.0979	15.317	239.67
2565	Mar	06.53988	Earth	0.0957	0.0934	0.0980	15.282	237.34
2610	Jul	23.66138	Vesta	0.0729	0.0721	0.0736	12.566	81.79
2686	Feb	26.91247	Earth	0.0902	0.0875	0.0930	17.314	250.46
2757	Feb	28.38681	Earth	0.0780	0.0778	0.0782	17.054	23.23
2991	Mar	08.92474	Earth	0.0916	0.0915	0.0918	15.084	12.51
3062	Mar	06.74113	Earth	0.0598	0.0580	0.0618	15.661	318.18
3133	Mar	07.85625	Earth	0.0652	0.0584	0.0733	15.510	1064.1
3183	Mar	02.73747	Earth	0.0776	0.0625	0.0954	17.099	1758.8
3254	Mar	05.33332	Earth	0.0530	0.0530	0.0540	16.140	686.39
3375	Mar	10.31755	Earth	0.0863	0.0858	0.0867	15.036	49.83
3454	Mar	04.25888	Earth	0.0719	0.0544	0.1412	16.918	6782.8
3504	Mar	04.69395	Earth	0.0723	0.0556	0.1484	16.906	7416.1
3575	Mar	10.79017	Earth	0.0785	0.0566	0.1178	15.141	4275.8
3625	Mar	06.10535	Earth	0.0588	0.0571	0.0678	16.343	1870.3

2005 CR37 close approaches using JPL orbit solution #30. This list of planetary encounters <0.1 AU terminates at the last Earth encounter prior to the linearized 3σ time of close approach uncertainty (TCA3Sg) exceeding ± 10 days. The nominal distance is the highest probability approach distance of the reference trajectory to the given body. Minimum and Maximum are the 3σ distances from the body at the nominal encounter time. V_{rel} is the nominal relative velocity. Integrations were performed using the DE403 planetary ephemeris and include relativistic perturbations due to the Sun, planets, and Moon, and asteroids Ceres, Pallas, and Vesta.

single Doppler and two ranges give a posteriori 3σ Doppler and range uncertainties of 3.3 Hz and 255 µs (38 km), reductions by factors of ~54 in Doppler frequency and ~1300 in time delay.

The interval over which the pre-radar orbit could be integrated reliably (defined by when the 3σ uncertainty in the time of Earth close-approach is $\leqslant \pm 10$ days, or the 3σ uncertainty in Earth close-approach distance at the nominal time of the encounter is $\leqslant \pm 0.1$ AU, whichever occurs first) was limited to 2005. Including the radar astrometry in a new orbit solution #30 (which includes 196 optical observations over 62 days along with the three radar measurements), the reliable close-approach prediction interval is extended to span 1784–3625, or about 1840 years (Table 2). Over that interval, the probability of Earth impact is effectively zero.

2. Photometric observations

One of us (D.P.) obtained photometry on 26 February 2005 at Carbuncle Hill Observatory (Rhode Island, USA) using a 0.35-m Schmidt–Cassegrain telescope equipped with a SBIG ST-10XME CCD. All images were taken through a "clear" filter and were calibrated using dark, bias, and flat field frames. The observations began at 2:30 UT and continued for slightly over 4 h. The asteroid's apparent motion was ~21 arcmin h^{-1}, so the observations were conducted in eight sessions in which

the asteroid's magnitude was measured relative to comparison stars in each of the session fields. To relate the magnitude levels between sessions, first or last frames were reduced using common comparison stars and the levels were adjusted for best agreement. The linkages are accurate to <0.01 magnitude in most cases, and the end-to-end drift probably is no more than a few hundredths of a magnitude.

Fig. 1 shows the lightcurve. When a lightcurve has an amplitude this large (~1 mag), it is nearly always symmetric with two similar maxima and two similar minima. Using this assumption and the Fourier analysis algorithm of Harris and Lupishko (1989), we obtain $P/2 = 3.244 \pm 0.016$ h. The possible drift of ± 0.03 in magnitude level from start to end affects the solution period by about ± 0.03 h, giving a total formal uncertainty of about ± 0.04 h. Doubling these values yields $P = 6.49 \pm 0.08$ h. It is not possible to state a formal error bar that includes allowance for the modest asymmetry of the lightcurve, but from experience with similar cases, it is not likely greater than ~0.2 h. Thus, we are confident that the period lies in the range 6.5 ± 0.3 h.

3. Shape, dimensions, and surface features

Our image sequence (Fig. 2) reveals an elongated and bifurcated shape with lobes that are round, have comparable dimen-

sions, and are separated by a pronounced "neck." The images span about one-fourth of a rotation in an interval of 96 min, implying a rotation period of roughly 6 h, which is consistent with the photometrically-derived rotation period of 6.5 h determined shortly after the radar observations concluded.

The echo bandwidth at Arecibo's transmitter frequency equals $27.7(D/P)\cos(\delta)$, where D is the asteroid's overall
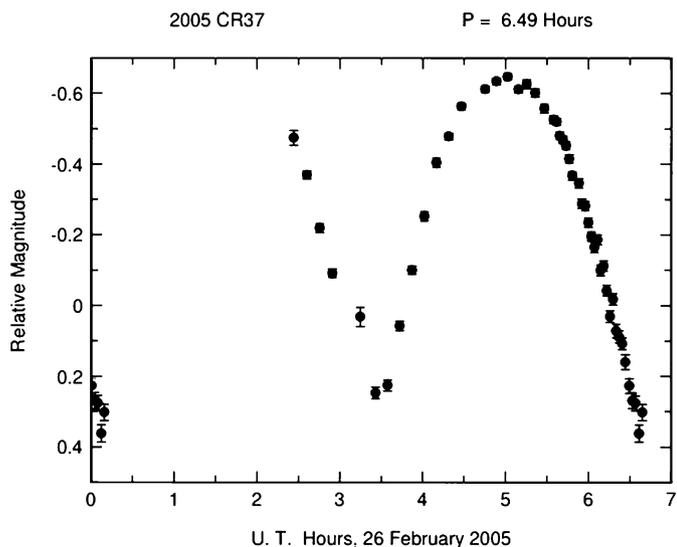

Fig. 1. 2005 CR37 lightcurve. Data plotted near 0 h UT are the last few points re-plotted one cycle earlier to show the size of the gap in phase coverage. Error bars are $\pm 1\sigma$.

plane-of-sky extent normal to the projected spin vector, δ is the subradar latitude, and P is the apparent rotation period. The echo bandwidth in the delay–Doppler images varies from 5.8 Hz in the most end-on orientation to 7.9 Hz broadside. However, noting that the orientation was closer to end-on at the start of the observations, we estimated the bandwidths from CW spectra processed to 0.1 Hz resolution and found that the minimum, 4.2 Hz, occurred during the first CW run. This places a lower bound on the elongation of $7.9/4.2 = 1.9$ and establishes that 2005 CR37 is a very elongated object, consistent with the 1-mag amplitude of the lightcurve. 2005 CR37's elongation, in the top one-third among those reported from radar observations (Table 3), is comparable to the elongations of 2063 Bacchus (Benner et al., 1999b) and 25143 Itokawa (Ostro et al., 2004, 2005a).

The first and last images in Fig. 2 have visible range extents of 1.1 km that establish a lower bound on the asteroid's longest dimension. The maximum bandwidth of 7.9 Hz and the 6.5 h rotation period constrain the lower bound on the maximum pole-on dimension, D_{max}, to be >1.8 km. When the asteroid is oriented broadside, the visible range extent of each lobe is about 0.4 km. If the true range extents are about twice the visible range extents, as would be true for a sphere, then each lobe is about 0.8 km deep in this orientation.

The images suggest that the asteroid's 2-D pole-on silhouette has extrema that are close to 1.8×0.8 km. If we pretend that its 3-D convex envelope is shaped like a biaxial ellipsoid, then its effective diameter (the diameter of a sphere with the same
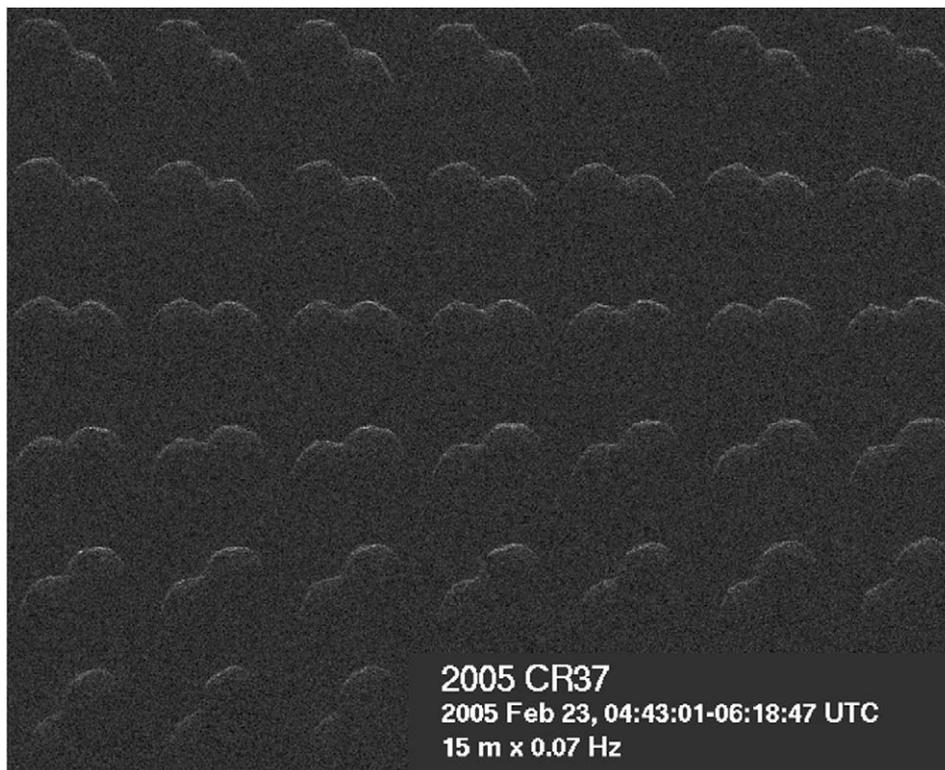

Fig. 2. 2005 CR37 radar movie. Our 1.6-h sequence of 38 runs is arranged chronologically, from left to right and top to bottom. Images are 64-s integrations separated by 80 s. Range increases from top to bottom and Doppler frequency increases from left to right, so rotation is counterclockwise. The resolution is 0.1 μs (15 m) × 0.07 Hz (∼14 m horizontally for an equatorial view). The images have the same logarithmic contrast stretch in order to take advantage of the dynamic range.

volume) is about 1 km. The actual effective diameter may be different due to concavities in the shape and the fact that the long axis may be longer than 1.8 km.

When oriented broadside, a valley with a depth of ∼150 m is visible between the lobes. The neck also has a visible range extent of about 150 m; if it's symmetric with respect to the asteroid's long axis, then its true extent would be about 300 m.

Table 3
NEA elongations from radar observations

Asteroid	Elongation	Reference
1620 Geographos	2.5	Hudson and Ostro (1999)
11066 Sigurd	2.5	Benner et al. (2004)
4179 Toutatis	2.4	Hudson and Ostro (1995)
433 Eros	2.2	Mitchell et al. (1998)
1627 Ivar	2.1	Ostro et al. (1990b)
2063 Bacchus	2.1	Benner et al. (1999b)
25143 Itokawa	1.9	Ostro et al. (2005a)
2005 CR37	>1.9	This paper
4183 Cuno	1.7	Benner et al. (2001)
4769 Castalia	1.6	Hudson and Ostro (1994)
1685 Toro	1.5	Ostro et al. (1983)
3103 Eger	1.5	Benner et al. (1997)
10115 1992 SK	1.5	Busch et al. (2006)
6178 1986 DA	1.4	Ostro et al. (1991)
6489 Golevka	1.4	Hudson et al. (2000a)
1862 Apollo	1.3	Ostro et al. (2002a)
2100 Ra-Shalom	1.2	Shepard et al. (2000)
3908 Nyx	1.2	Benner et al. (2002b)
4197 1982 TA	1.2	Ostro et al., unpublished
7822 1991 CS	1.2	Benner et al. (1999a)
1998 KY26	1.2	Ostro et al. (1999)
53319 1999 JM8	1.2	Benner et al. (2002a)
1999 RQ36	1.2	Hudson et al. (2000b)
1580 Betulia	1.1	Magri et al., in preparation
1998 ML14	1.1	Ostro et al. (2001)

NEA elongations estimated from three-dimensional shape inversions, convex hulls, or bandwidth extrema. For the non-principal axis rotator Toutatis, we list the ratio of the long to the intermediate axis from its shape model. For objects described in more than one reference (Castalia, Geographos, Toutatis, Ra-Shalom, and Itokawa), the most recent estimate of the elongation is cited.

Let us denote the left and right lobes in the images as Alpha and Beta. Fig. 3 shows a collage of three enlarged images. Images obtained over a range of rotation phases show that the edge of Alpha adjacent to the neck appears angular, suggesting the presence of at least one facet. The facet is slightly raised away from the surface (Fig. 3A). Portions of Beta also appear to be faceted in images when Beta was closer to Earth than Alpha (Fig. 3C).

Other irregularities are present along the leading edge. In multiple images, a "hill" consisting of several pixels in delay is evident in the middle of Alpha's leading edge (Figs. 3B and 3C). The sequence in Fig. 3 suggests that the "hill" may be one end of the "raised facet" described above. Near the "neck," another feature visible in multiple images shows a curve of moderately bright pixels that partially bound an inner radar-dark region (Fig. 3B). A similar feature is evident in several images of Beta's leading edge (Fig. 3C). These features give the impression of obliquely-viewed concavities, perhaps craters, and are similar to features seen on 53319 1999 JM8 (Benner et al., 2002a).

A number of images also show a cluster of diffuse pixels located about 150 m behind Alpha's leading edge (arrow in Figs. 3A and 3C). They are faint in many frames but are more conspicuous when the images are shown as an animation (see the supplementary online material). We interpret this feature as a modest topographic high that is barely visible due to the observing geometry. Another cluster of faint pixels appears on Beta in the last several frames and may also represent a positive relief feature.

4. Disc-integrated radar and optical properties

Table 4 lists estimates of the asteroid's radar cross section, which for this experiment could be obtained most reliably from the CW spectra (Fig. 4). The cross sections show a steady increase as a function of time, a pattern that matches the progression of increasing surface area oriented toward the radar in the
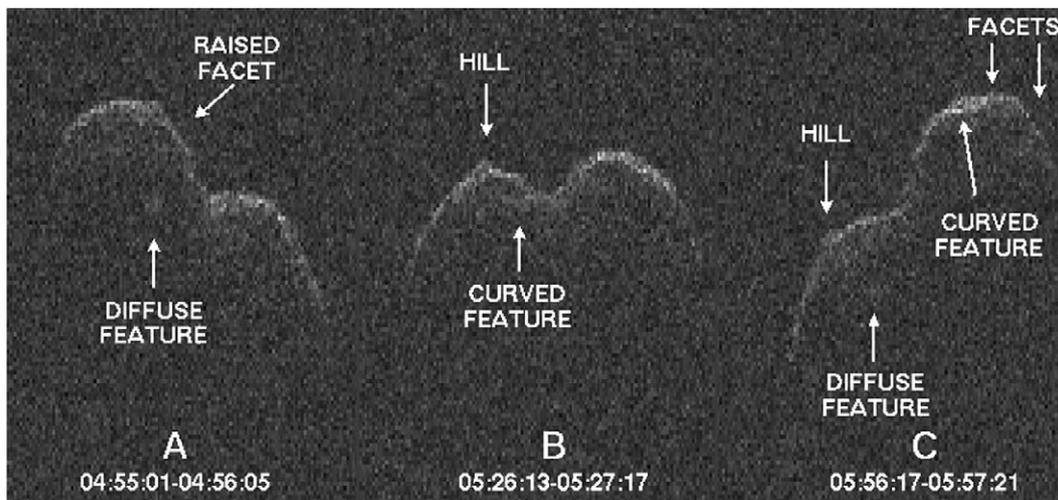

Fig. 3. Enlarged images of three runs from the beginning (A), middle (B), and end (C) of the track. Delay–Doppler extents and orientations are the same as in Fig. 2. Arrows indicate features described in the text. Times spanned by each image are given at the bottom. The images have the same logarithmic contrast stretch in order to take advantage of the dynamic range.

Table 4
Radar properties

Run	$\sigma_{OC} \pm 25\%$ (km^2)	SC/OC
1	0.14	0.33 ± 0.01
2	0.15	0.28 ± 0.01
3	0.16	0.31 ± 0.01
4	0.17	0.31 ± 0.01
5	0.17	0.37 ± 0.01
6	0.19	0.30 ± 0.01
Mean	0.16	0.32 ± 0.03

σ_{OC} is the OC radar cross section; uncertainties are dominated by systematic pointing and calibration errors. The cross sections and SC/OC were estimated using a frequency resolution of 0.5 Hz in order to have enough fast-Fourier transforms ($N = 60$) to produce nearly Gaussian noise statistics. For SC/OC, systematic effects cancel and most remaining statistical errors propagate from receiver thermal noise. The last row lists the mean for σ_{OC} and the mean and rms dispersion for SC/OC.

images obtained shortly after the CW observations. This partial radar "lightcurve" is reminiscent of those obtained from 433 Eros (Jurgens and Goldstein, 1976), 1685 Toro (Ostro et al., 1983), 1620 Geographos (Ostro et al., 1996), and 7822 1991 CS (Benner et al., 1999a).

The radar cross section from the sixth run was obtained when the asteroid was oriented close to mid-way between end-on and broadside. As such, it represents a first-order estimate of the average cross section, so let us adopt it as our nominal value and explore its implications.

If we adopt an effective diameter of 1 km, then a radar cross section of 0.19 km^2 yields a relatively bright radar albedo of $\sim$0.2 that is comparable to those obtained from several other NEAs. The radar brightness could be explained by a low near-surface porosity (i.e., relatively high near-surface density; Magri et al., 2001).

The circular polarization ratios of the spectra have a mean and rms dispersion of 0.32 ± 0.03, which is indistinguishable from the average observed from other radar-detected NEAs. This indicates that the near-surface is moderately complex at decimeter scales (Ostro et al., 2002b). Strong OC-only glints in runs 3, 4, and 6 may partly explain the dispersion in SC/OC (Fig. 4). Glints are also visible on the leading edge in several delay–Doppler images when the contrast has been stretched appropriately; when taken as a whole, the glints are consistent with the presence of facets that are evident in the delay–Doppler images, since large facets that are smooth at decimeter scales produce quasi-specular OC-only radar reflections.

5. Discussion

Facets spanning lengths from tens of meters to more than 1 km are evident in radar images of 1620 Geographos (Ostro et al., 1996), 4179 Toutatis (Ostro et al., 1995), 6489 Golevka (Hudson et al., 2000a), 53319 1999 JM8 (Benner et al., 2002a), 54509 2000 PH5 (Taylor et al., 2004), and 11066 Sigurd (Benner et al., 2004), but the raised facet on 2005 CR37 is unlike any seen in radar images of other asteroids.

This asteroid clearly is bifurcated, but since our rotation-phase coverage is limited (and certainly insufficient for 3-D
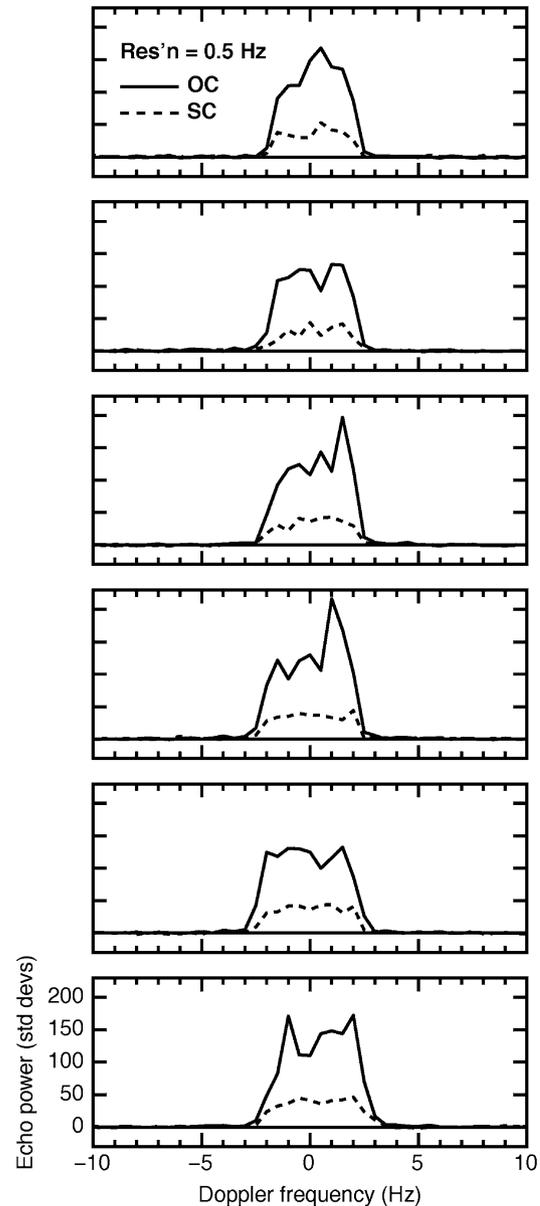

Fig. 4. Echo power spectra from each run, shown at 0.5-Hz resolution, arranged chronologically from top to bottom.

shape reconstruction), we do not know if the concavity between Alpha and Beta is a waist that encircles the long axis, in which case we should arguably describe the asteroid as having a "contact binary shape," or just a "dent" fortuitously seen in our images. Hence we designate 2005 CR37 as a candidate for actually being a contact binary (an asteroid consisting of two lobes that are in contact, have a bimodal mass distribution, and that may once have been separate). We do not take the term "contact binary" to imply that the two components are in a Keplerian orbit with surfaces that almost touch. Very close orbits are unstable against tidal evolution and will eventually collapse to form a shape such as 2005 CR37's or expand to resemble a true binary system such as 69230 Hermes (Weidenschilling et al., 1989; Margot et al., 2003). Furthermore, even if tidal friction is ignored, for slowly-orbiting pairs that almost touch, the bulk

densities required to maintain Keplerian orbits by comparably-sized objects would be unphysically low.

Table 5 lists estimates of the dimensions and rotation periods of candidate contact binary NEAs imaged by radar including: 4769 Castalia (Ostro et al., 1990a; Hudson and Ostro, 1994), 2063 Bacchus (Benner et al., 1999b), 4486 Mithra (Ostro et al., 2000), 11066 Sigurd (Benner et al., 2004), 2002 NY40 (Pravec et al., 2005). Although 4179 Toutatis is sometimes referred to as a contact binary, we do not consider it a candidate for being one because its mass distribution is not bimodal (Hudson and Ostro, 1995; Hudson et al., 2003). 2005 CR37 has dimensions that are comparable to those of Castalia, 2001 KZ66, and perhaps 1993 OM7. Its rotation period is the third fastest among those listed in the table.

Scheeres et al. (2004) have shown that the spins of elongated NEAs can be slowed and can be "excited" into non-principal axis (NPA) states by tidal interactions during close encounters with Earth and Venus. However, the YORP effect may be a more likely explanation for slow rotation (Bottke et al., 2002). A possible implication is that a rapidly rotating object such as 2005 CR37 may be relatively young while a slowly rotating, NPA rotator such as Mithra may be relatively old. In other words, elongated objects that rotate rapidly may not have had sufficient time for YORP or close flybys to alter their spin and place them into NPA rotation states.

The images of 2005 CR37 were obtained at a resolution equal to or higher than those of other candidate contact binaries, and they reveal an object with more surface structure than is evident on the other objects. The only other candidate contact binary imaged at comparable range and Doppler resolutions is 2002 NY40.

How did the shape of 2005 CR37 originate? Mechanisms thought capable of forming contact binaries include low-velocity collisions (Farinella, 1992; Hudson and Ostro, 1995; Chauvineau et al., 1995; Bottke and Melosh, 1996a, 1996b; Leinhardt et al., 2000), perhaps between components of true binaries, and spinup and shape distortion of gravitationally-bound agglomerates via either very close encounters with Earth and Venus (Asphaug and Benz, 1996; Richardson et al., 1998) or asymmetric solar absorption and re-emission (YORP; Bottke et al., 2002). Other explanations, such as a sequence of impacts that sculpted the object into its present shape, or an origin as an impact shard from catastrophic disruption of a larger progenitor, seem more contrived.

Is 2005 CR37 an ex-binary? Consider the following thought experiment. If we "pull apart" the asteroid into two components with the same angular momentum, then we can produce a synchronous pair with an orbital period of about 14 h, a spin–orbit state very similar to that of Hermes (Margot et al., 2003; Pravec et al., 2005). In other words, 2005 CR37 could have been like Hermes. Alternatively, 2005 CR37 could split into two objects due to modest effects from YORP or close planetary flybys.

Now consider the situation if 2005 CR37's components were in a Keplerian orbit so that the surfaces almost touched. If the two components were free to drift apart, they would evolve outward toward a synchronous state like Hermes through tidal friction and the binary form of YORP (Cuk and Burns, 2005). Consequently, the two components must be in a state of compression, so we can place a lower bound on their bulk density in order that gravity exceeds the centrifugal force. If we assume the components have equal diameters and masses and we adopt $a/R = 1.9$ (where a is their separation and R is the diameter of each component), so the components are slightly "squished," then 6.5-h rotation period places a lower bound on the bulk density of ~ 1 g cm^{-3}.

How did the structural complexity on 2005 CR37 originate? For a contact binary formed by a low-velocity collision, morphologically complex terrain near the intersection of the lobes, as is seen on this object, may be almost inevitable. This may explain the raised facet, which we speculate could be a fault block formed by compressional stresses during an impact.

The complex surface morphology on 2005 CR37 is somewhat more rugged than the generally smooth shapes produced by simulations of collisions or tidal distortion of agglomer-

Table 5
Candidate contact binary NEAs

Asteroid	Diameter (km)	Res'n (m)	Rotation period (h)		Reference
68346 2001 KZ66	1.0	15	2.7		Nolan et al., unpublished
4769 Castalia	1.0	300	4[a]		Ostro et al. (1990a); Hudson and Ostro (1994)
2005 CR37	1.0	15	6.5		This paper
11066 Sigurd	3.0	75	8.5[b,c]		Benner et al. (2004)
2063 Bacchus	0.6	75	15.1[b]		Benner et al. (1999b)
2002 NY40	0.4	15	20[d]	NPA	Pravec et al. (2005)
4486 Mithra	2.4	19	$\sim$100[d]	NPA	Ostro et al. (2000)
2002 FC	0.7	15	days		Ostro et al., unpublished
52387 1993 OM7	1.0	15	Weeks		Ostro et al., unpublished
2004 RF84	2.4	15	Weeks		Benner et al., unpublished

Candidate contact binary NEAs imaged by delay–Doppler radar observations. "Res'n" indicates the range resolution of delay–Doppler radar images. "NPA" indicates non-principal axis rotation. The objects are listed in order of increasing rotation period. Rotation periods with footnotes are from the references cited; we estimated the other periods from sequences of unpublished radar images.

[a] Ostro et al. (1990a).
[b] Pravec et al. (1998).
[c] Krugly et al. (2002).
[d] Pravec et al. (2005).

ates of gravitationally-bound spheres (Richardson et al., 1998; Leinhardt et al., 2000). The raised facet suggests to us that 2005 CR37 might be at least partially fractured and hence not monolithic. Perhaps its internal structure consists of an assemblage of irregularly-shaped blocks that span a distribution of sizes. Simulations of collisions or tidal distortion by such assemblages may clarify the various possibilities.

How abundant are contact binaries in the NEA population? Since January 1999, about 9% of radar-imaged NEAs larger than ~200 m have bifurcated shapes and can be considered candidate contact binaries (two possible contact binaries were imaged by radar prior to 1999: 4769 Castalia and 2063 Bacchus). The abundance of true binaries above the same size threshold imaged by radar during the same interval is about 17% (Margot et al., 2002; Merline et al., 2002; Pravec et al., 2005). If contact binaries and true binaries form by the same mechanisms, as has been suggested theoretically, then both types of objects should exist. Is there really a two-fold difference in the abundance of binaries and contact binaries in the NEA population?

The processes that make binary NEAs evidently produce a wide range of primary and secondary diameters and diameter ratios (Merline et al., 2002; Ostro et al., 2002b; Pravec et al., 2006), with binaries that have comparably-sized components (such as Hermes) representing one "corner" of the distribution. Some binaries presumably evolve inward and collide to form objects like 2005 CR37. If binary components have size-frequency distributions similar to those of collisional fragments, then relatively small secondaries should be much more abundant than comparably-sized secondaries, in general agreement with the trend observed photometrically and by radar. In a sense, there are simply more ways to be unequal rather than equal in size. Radar imaging at higher SNRs might reveal significantly more binary systems with smaller secondary/primary diameter ratios than are presently observed. 1862 Apollo is a notable example: recent Arecibo radar imaging revealed a satellite only ~75 m in diameter (± a factor of two) and a nominal secondary/primary ratio of ~0.05 (Ostro et al., 2005b). Thus, the current factor-of-two difference between the abundance of true binaries and contact binaries may be biased.

Which way is the evolution of 2005 CR37 going? Is 2005 CR37 a failed binary that collapsed back into a single object? Or is it a rubble pile being spun up by YORP or planetary tides that is on the verge of fission into a true binary?

Acknowledgments

Supplementary material

Supplementary data associated with this article can be found, in the online version, at doi:10.1016/j.icarus.2006.01.016.

References

Asphaug, E., Benz, W., 1996. Size, density, and structure of Comet Shoemaker–Levy 9 inferred from the physics of tidal breakup. Icarus 121, 225–248.

Benner, L.A.M., Ostro, S.J., Giorgini, J.D., Jurgens, R.F., Mitchell, D.L., Rose, R., Rosema, K.D., Slade, M.A., Winkler, R., Yeomans, D.K., Campbell, D.B., Chandler, J.F., Shapiro, I.I., 1997. Radar detection of near-Earth Asteroids 2062 Aten, 2101 Adonis, 3103 Eger, 4544 Xanthus, and 1992 QN. Icarus 130, 296–312.

Benner, L.A.M., Ostro, S.J., Rosema, K.D., Giorgini, J.D., Choate, D., Jurgens, R.F., Rose, R., Slade, M.A., Thomas, M.L., Winkler, R., Yeomans, D.K., 1999a. Radar observations of Asteroid 7822 (1991 CS). Icarus 137, 247–259.

Benner, L.A.M., Hudson, R.S., Ostro, S.J., Rosema, K.D., Giorgini, J.D., Yeomans, D.K., Jurgens, R.F., Mitchell, D.L., Winkler, R., Rose, R., Slade, M.A., Thomas, M.L., 1999b. Radar observations of Asteroid 2063 Bacchus. Icarus 139, 309–327.

Benner, L.A.M., Nolan, M.C., Margot, J.L., Giorgini, J.D., Hudson, R.S., Jurgens, R.F., Ostro, S.J., 2001. Recent radar observations of four near-Earth asteroids. Bull. Am. Astron. Soc. 33, 918. Abstract.

Benner, L.A.M., Ostro, S.J., Nolan, M.C., Margot, J.L., Giorgini, J.D., Hudson, R.S., Jurgens, R.F., Slade, M.A., Howell, E.S., Campbell, D.B., Yeomans, D.K., 2002a. Radar observations of Asteroid 1999 JM8. Meteorit. Planet. Sci. 37, 779–792.

Benner, L.A.M., Ostro, S.J., Hudson, R.S., Rosema, K.D., Jurgens, R.F., Yeomans, D.K., Campbell, D.B., Chandler, J.F., Shapiro, I.I., 2002b. Radar observations of Asteroid 3908 Nyx. Icarus 158, 379–388.

Benner, L.A.M., Nolan, M.C., Carter, L.M., Ostro, S.J., Giorgini, J.D., Magri, C., Margot, J.L., 2004. Radar imaging of near-Earth Asteroid 11066 Sigurd. Bull. Am. Astron. Soc. 36. Abstract #32.29.

Bottke, W.F., Melosh, H.J., 1996a. Formation of asteroid satellites and doublet craters by planetary tidal forces. Nature 381, 51–53.

Bottke, W.F., Melosh, H.J., 1996b. Binary asteroids and the formation of doublet craters. Icarus 124, 372–391.

Bottke, W.F., Vokrouhlicky, D., Rubincam, D.P., Broz, M., 2002. The effect of Yarkovsky thermal forces on the dynamical evolution of asteroids and meteoroids. In: Bottke, W.F., Cellino, A., Paolicchi, P., Binzel, R.P. (Eds.), Asteroids III. Univ. of Arizona Press, Tucson, pp. 395–408.

Busch, M.W., Ostro, S.J., Benner, L.A.M., Giorgini, J.D., Jurgens, R.F., Rose, R., Magri, C., Pravec, P., Scheeres, D.J., Broschart, S.B., 2006. Radar and optical observations and physical modeling of near-Earth Asteroid 10115 (1992 SK). Icarus 181, 145–155.

Chauvineau, B., Farinella, P., Harris, A.W., 1995. The evolution of Earth-approaching binary asteroids: A Monte Carlo dynamical model. Icarus 115, 36–46.

Cuk, M., Burns, J.A., 2005. Effects of thermal radiation on the dynamics of binary NEAs. Icarus 176, 418–431.

Farinella, P., 1992. Evolution of Earth-crossing binary asteroids due to gravitational encounters with the Earth. Icarus 96, 284–285.

Harris, A.W., Lupishko, D.F., 1989. Photometric lightcurve observations and reduction techniques. In: Binzel, R.P., Gehrels, T., Matthews, M.S. (Eds.), Asteroids II. Univ. of Arizona Press, Tucson, pp. 39–53.

Hudson, R.S., Ostro, S.J., 1994. Shape of Asteroid 4769 Castalia (1989 PB) from inversion of radar images. Science 263, 940–943.

Hudson, R.S., Ostro, S.J., 1995. Shape and non-principal axis spin state of Asteroid 4179 Toutatis. Science 270, 84–86.

Hudson, R.S., Ostro, S.J., 1999. Physical model of Asteroid 1620 Geographos from radar and optical data. Icarus 140, 369–378.

Hudson, R.S., Ostro, S.J., Jurgens, R.F., Rosema, K.D., Giorgini, J.D., Winkler, R., Rose, R., Choate, D., Cormier, R.A., Franck, C.R., Frye, R., Howard, D., Kelley, D., Littlefair, R., Slade, M.A., Benner, L.A.M., Thomas, M.L., Mitchell, D.L., Chodas, P.W., Yeomans, D.K., Scheeres, D.J., Palmer, P., Zaitsev, A., Koyama, Y., Nakamura, A., Harris, A.W., Meshkov, M.N., 2000a. Radar observations and physical model of Asteroid 6489 Golevka. Icarus 148, 37–51.

Hudson, R.S., Ostro, S.J., Benner, L.A.M., 2000b. Recent delay–Doppler radar asteroid modeling results: 1999 RQ36 and craters on Toutatis. Bull. Am. Astron. Soc. 32, 1001. Abstract.

Hudson, R.S., Ostro, S.J., Scheeres, D.J., 2003. High-resolution model of Asteroid 4179 Toutatis. Icarus 161, 346–355.

Jurgens, R.F., Goldstein, R.M., 1976. Radar observations at 3.5 and 12.6 cm wavelength of Asteroid 433 Eros. Icarus 28, 1–15.

Krugly, Y.N., Belskaya, I.N., Shevchenko, V.G., Chiorny, V.G., Velichko, F.P., Mottola, S., Erikson, A., Hahn, G., Nathues, A., Neukum, G., Gaftonyuk, N.M., Dotto, E., 2002. The near-Earth objects followup program. IV. CCD photometry in 1996–1999. Icarus 158, 294–304.

Leinhardt, Z.M., Richardson, D.C., Quinn, T., 2000. Direct N-body simulations of rubble pile collisions. Icarus 146, 133–151.

Magri, C., Consolmagno, G.J., Ostro, S.J., Benner, L.A.M., Beeney, B.R., 2001. Radar constraints on asteroid regolith compositions using 433 Eros as ground truth. Meteorit. Planet. Sci. 36, 1697–1709.

Margot, J.L., Nolan, M.C., Benner, L.A.M., Ostro, S.J., Jurgens, R.F., Giorgini, J.D., Slade, M.A., Campbell, D.B., 2002. Binary asteroids in the near-Earth object population. Science 296, 1445–1448.

Margot, J.L., Nolan, M.C., Negron, V., Hine, A.A., Campbell, D.B., Howell, E.S., Benner, L.A.M., Ostro, S.J., Giorgini, J.D., 2003. 1937 UB (Hermes). IAU Circ. 8227.

Merline, W.J., Weidenschilling, S.J., Durda, D.D., Margot, J.L., Pravec, P., Storrs, A.D., 2002. Asteroids do have satellites. In: Bottke, W.F., Cellino, A., Paolicchi, P., Binzel, R.P. (Eds.), Asteroids III. Univ. of Arizona Press, Tucson, pp. 289–312.

Mitchell, D.L., Hudson, R.S., Ostro, S.J., Rosema, K.D., 1998. Shape of Asteroid 433 Eros from inversion of Goldstone radar Doppler spectra. Icarus 131, 4–14.

Ostro, S.J., Campbell, D.B., Shapiro, I.I., 1983. Radar observations of Asteroid 1685 Toro. Astron. J. 88, 565–576.

Ostro, S.J., Chandler, J.F., Hine, A.A., Rosema, K.D., Shapiro, I.I., Yeomans, D.K., 1990a. Radar images of Asteroid 1989 PB. Science 248, 1523–1528.

Ostro, S.J., Campbell, D.B., Hine, A.A., Shapiro, I.I., Chandler, J.F., Werner, C.L., Rosema, K.D., 1990b. Radar images of Asteroid 1627 Ivar. Astron. J. 99, 2012–2018.

Ostro, S.J., Campbell, D.B., Chandler, J.F., Hine, A.A., Hudson, R.S., Rosema, K.D., Shapiro, I.I., 1991. Asteroid 1986 DA: Radar evidence for a metallic composition. Science 252, 1399–1404.

Ostro, S.J., Hudson, R.S., Jurgens, R.F., Rosema, K.D., Campbell, D.B., Yeomans, D.K., Chandler, J.F., Giorgini, J.D., Winkler, R., Rose, R., Howard, S.D., Slade, M.A., Perillat, P., Shapiro, I.I., 1995. Radar images of Asteroid 4179 Toutatis. Science 270, 80–83.

Ostro, S.J., Jurgens, R.F., Rosema, K.D., Hudson, R.S., Giorgini, J.D., Winkler, R., Yeomans, D.K., Choate, D., Rose, R., Slade, M.A., Howard, S.D., Scheeres, D.J., Mitchell, D.L., 1996. Radar observations of Asteroid 1620 Geographos. Icarus 121, 46–66.

Ostro, S.J., Pravec, P., Benner, L.A.M., Hudson, R.S., Sarounova, L., Hicks, M.D., Rabinowitz, D.L., Scotti, J.V., Tholen, D.J., Wolf, M., Jurgens, R.F., Thomas, M.L., Giorgini, J.D., Chodas, P.W., Yeomans, D.K., Rose, R., Frye, R., Rosema, K.D., Winkler, D.K., Slade, M.A., 1999. Radar and optical observations of Asteroid 1998 KY26. Science 285, 557–559.

Ostro, S.J., Hudson, R.S., Benner, L.A.M., Nolan, M.C., Margot, J.L., Giorgini, J.D., Jurgens, R.F., Rose, R., Yeomans, D.K., 2000. Radar observations of Asteroid 4486 Mithra. Bull. Am. Astron. Soc. 32, 1003. Abstract.

Ostro, S.J., Hudson, R.S., Benner, L.A.M., Nolan, M.C., Giorgini, J.D., Scheeres, D.J., Jurgens, R.F., Rose, R., 2001. Radar observations of Asteroid 1998 ML14. Meteorit. Planet. Sci. 36, 1225–1236.

Ostro, S.J., Rosema, K.D., Campbell, D.B., Shapiro, I.I., 2002a. Radar observations of Asteroid 1862 Apollo. Icarus 156, 580–583.

Ostro, S.J., Hudson, R.S., Benner, L.A.M., Giorgini, J.D., Magri, C., Margot, J.L., Nolan, M.C., 2002b. Asteroid radar astronomy. In: Bottke, W.F., Cellino, A., Paolicchi, P., Binzel, R.P. (Eds.), Asteroids III. Univ. of Arizona Press, Tucson, pp. 151–168.

Ostro, S.J., Benner, L.A.M., Nolan, M.C., Magri, C., Giorgini, J.D., Scheeres, D.J., Broschart, S.B., Kaasalainen, M., Vokrouhlicky, D., Chesley, S.R., Margot, J.L., Jurgens, R.F., Rose, R., Yeomans, D.K., Suzuki, S., DeJong, E.M., 2004. Radar observations of Asteroid 25143 Itokawa (1998 SF36). Meteorit. Planet. Sci. 39, 407–424.

Ostro, S.J., Benner, L.A.M., Magri, C., Giorgini, J.D., Rose, R., Jurgens, R.F., Yeomans, D.K., Hine, A.A., Nolan, M.C., Scheeres, D.J., Kaasalainen, M., Vokrouhlicky, D., Chesley, S.R., Margot, J.L., 2005a. Radar observations of Itokawa in 2004 and improved shape modeling. Meteorit. Planet. Sci. 41, 1563–1574.

Ostro, S.J., Benner, L.A.M., Giorgini, J.D., Nolan, M.C., Hine, A.A., Howell, E.S., Margot, J.L., Magri, C., Shepard, M.K., 2005b. 1862 Apollo. IAU Circ. 8627.

Pravec, P., Wolf, M., Sarounova, S., 1998. Lightcurves for 26 near-Earth asteroids. Icarus 136, 124–136.

Pravec, P., Harris, A.W., Scheirich, P., Kusnirak, P., Sarounova, L., Hergenrother, C.W., Mottola, S., Hicks, M.D., Masri, G., Krugly, Y.N., Shevchenko, V.G., Nolan, M.C., Howell, E.S., Kaasalainen, M., Galad, A., Brown, P., DeGraff, D.R., Lambert, J.V., Cooney, W.R., Foglia, S., 2005. Tumbling asteroids. Icarus 173, 108–131.

Pravec, P., Scheirich, P., Kusnirak, P., Sarounova, L., Mottola, S., Hahn, G., Brown, P., Esquerdo, G., Kaiser, N., Krzeminski, Z., Pray, D.P., Warner, B.D., Nolan, M.C., Howell, E.S., Benner, L.A.M., Harris, A.W., Galad, A., Holliday, W., Hicks, M.D., Krugly, Y.N., Tholen, D., Whiteley, R., Marchis, F., DeGraff, D.R., Grauer, A., Larson, S., Velichko, F.P., Cooney, W.R., Stephens, R., Zhu, J., Kirsch, K., Dyvig, R., Snyder, L., Reddy, V., Moore, S., Gajdos, S., Vilagi, J., Masi, G., Higgins, D., Funkhouser, G., Knight, B., Slivan, S., Behrend, R., Roy, R., Demeautis, C., Matter, D., Waelchli, N., Revaz, Y., Klotz, A., Rieugne, M., Thierry, P., Cotrez, V., Brunetto, L., Kober, G., 2006. Photometric survey of binary near-Earth asteroids. Icarus 181, 63–93.

Richardson, D.C., Bottke, W.F., Love, S.G., 1998. Tidal distortion and disruption of Earth-crossing asteroids. Icarus 134, 47–76.

Scheeres, D.J., Marzari, F., Rossi, A., 2004. Evolution of NEO rotation rates due to close encounters with Earth and Venus. Icarus 170, 312–323.

Shepard, M.K., Ostro, S.J., Benner, L.A.M., Harris, A.W., Rosema, K.D., Shapiro, I.I., Chandler, J.F., Campbell, D.B., 2000. Radar observations of 2100 Ra-Shalom. Icarus 147, 520–529.

Taylor, P.A., Margot, J.L., Nicholson, P.D., Campbell, D.B., Jurgens, R.F., Ostro, S.J., Benner, L.A.M., Giorgini, J.D., Nolan, M.C., Howell, E.S., Hine, A.A., Hudson, R.S., 2004. Properties of horseshoe object 2000 PH5 from radar observations. Bull. Am. Astron. Soc. 36, 1181. Abstract.

Weidenschilling, S.J., Paolicchi, P., Zappala, V., 1989. Do asteroids have satellites? In: Binzel, R.P., Gehrels, T., Matthews, M.S. (Eds.), Asteroids II. Univ. of Arizona Press, Tucson, pp. 643–658.